

Hard X-ray Luminosities of Multinuclei Infrared Luminous Galaxies Showing a Radio/Far-Infrared Excess

Masatoshi Imanishi ¹

National Astronomical Observatory, Mitaka, Tokyo 181-8588, Japan

and

Shiro Ueno ²

Department of Physics and Astronomy, University of Leicester, University Road, Leicester
LE1 7RH, UK

ABSTRACT

We report the results of hard X-ray observations of four multinuclei merging infrared luminous galaxies (IRLGs). We selected these four sources for their excess of radio to far-infrared luminosity ratio compared with starburst galaxies. This excess suggests that activity associated with a supermassive black hole (SMBH) contributes strongly to the IRLGs' bolometric luminosities. Although we expect strong hard X-ray emission from the SMBH-driven activity, the radio-excess multinuclei merging IRLGs show considerably smaller hard X-ray luminosities relative to far-infrared (40–500 μm) and infrared (8–1000 μm) luminosities than active galactic nuclei (AGNs) showing a similar radio-excess. This result may demonstrate that emission in the hard X-ray region from SMBH-driven activity in the multinuclei merging IRLGs is severely suppressed compared to a typical spectral energy distribution of SMBH-driven activity in AGNs. If this is a common property of merging IRLGs, without its correction, hard X-ray observations underestimate the contribution of SMBH-driven activity to the bolometric luminosities of merging IRLGs.

Subject headings: galaxies: active — X-rays: galaxies — radio: galaxies

¹Present address: Institute for Astronomy, University of Hawaii, 2680 Woodlawn Drive, Honolulu, Hawaii 96822, USA

²Present address: Space Utilization Research Program, Tsukuba Space Center, National Space Development Agency of Japan, 2-1-1 Sengen, Tsukuba 305-8505, Japan

1. Introduction

Infrared luminous galaxies (IRLGs) radiate most of their extreme luminosities in the far-infrared (FIR; $40\text{--}500\ \mu\text{m}$; $L_{\text{FIR}} > 10^{11.25} L_{\odot}$; $H_0 = 75\ \text{km s}^{-1}\ \text{Mpc}^{-1}$, $q_0 = 0.5$). Most of these sources are thought to be in some stage of a merger process of molecular gas-rich galaxies and to evolve into active galactic nuclei (AGNs) after the merger (Sanders et al. 1988a; Hutchings & Neff 1991). In IRLGs, two types of activity are thought to occur: one associated with a supermassive black hole (SMBH) and the other, with a starburst (e.g., Sanders & Mirabel 1996). Which of the two types of activity, starburst or SMBH, is the dominant energy source is a fundamental issue in the study of IRLGs.

Since the UV to soft X-ray ionizing photons are the main power source of SMBH-driven activity, measuring the UV to soft X-ray luminosities of SMBH-driven activity is the most direct way to estimate the contribution of SMBH-driven activity to the bolometric luminosities of galaxies. However, direct measurements of the UV to soft X-ray luminosity of SMBH-driven activity is practically impossible in IRLGs because of high attenuation by the abundant dust in IRLGs. Therefore, other less-direct methods have been employed to estimate the contribution of SMBH-driven activity to the bolometric luminosities.

One such method is hard X-ray observations; following convention, we refer to the 2–10 keV energy band as hard X-rays throughout this paper. Since the effect of extinction is small in the hard X-ray region, SMBH-driven activities should be detectable even through thick obscuring material, up to $N_{\text{H}} \sim 10^{24}\ \text{cm}^{-2}$. Further, the hard X-ray luminosities relative to far-infrared luminosities ($L_{\text{X}}/L_{\text{FIR}}$) in AGNs ($\gtrsim 0.1$) are 2–3 orders of magnitude higher than those in starburst galaxies ($\sim 10^{-3}$; Tsuru 1992). The strong hard X-ray emission from AGNs is thought to originate from SMBH-driven activity. If SMBH-driven activity in IRLGs has the same hard X-ray emission efficiency as that in AGNs, the main energy source of IRLGs should be easily discernible from the intrinsic hard X-ray luminosities. Hard X-ray observations of IRLGs have been made and no strong hard X-ray emission has been found (i.e., $L_{\text{X}}/L_{\text{FIR}} < 0.05$; Ueno et al. 1996; Nakagawa et al. 1997; Ogasaka et al. 1997; Brandt et al. 1997; Iwasawa 1999). These results can be explained if the IRLGs are powered by starburst activity rather than SMBH-driven activity, or if the direct hard X-ray emission from SMBH-driven activity is completely blocked by thick ($N_{\text{H}} > 10^{24}\ \text{cm}^{-2}$) absorbing gas. However, many IRLGs are thought to be powered by SMBH-driven activity based on near-infrared (Veilleux et al. 1997b) and mid-infrared diagnostics (Genzel et al. 1998), both of which suggest huge UV to soft X-ray emission from SMBH-driven activity in these IRLGs. Some of such IRLGs have been observed with hard X-rays (e.g., IRAS F20460+1925; Ogasaka et al. 1997; IRAS F23060+0505; Brandt et al. 1997; Mrk 231; Iwasawa 1999; Mrk 463; Ueno et al. 1996). Although direct hard X-ray emission is

thought to be detected based on the spectral shape, the extinction-corrected hard X-ray luminosities are much smaller than that expected if they are powered by SMBH-driven activity. This may indicate that the intrinsic hard X-ray luminosities relative to UV to soft X-ray luminosities from SMBH-driven activities in IRLGs are considerably smaller than those in AGNs. In other words, even if strong UV to soft X-ray emission from SMBH-driven activity exists, hard X-ray emission from SMBH-driven activity may not develop during the early phase of a merger as much as during the later or final stages of a merger (Imanishi & Ueno 1999).

To investigate the possible hard X-ray underluminosity (relative to other spectral regions) of SMBH-driven activity during a merger, we performed hard X-ray observations of merging IRLGs that are thought to possess strong SMBH-driven activities.

2. Targets

To select merging IRLGs possessing strong SMBH-driven activity, we use the radio to far-infrared luminosity ratio. In galaxies where starburst activity is thought to be a predominant energy source, the distribution of radio 1.5 GHz (= 20 cm) to far-infrared luminosity ratios is very narrow. If we use the q -value introduced by Helou, Soifer, & Rowan-Robinson (1985),

$$q \equiv \log(f_{\text{FIR}}/f_{20\text{cm}})$$

$$f_{\text{FIR}} = 0.336 \times (2.58 \times f_{60\mu\text{m}} + f_{100\mu\text{m}}),$$

where f_x means flux at wavelengths “x” in units of Jy, q -values of starburst galaxies are $q = 2.34 \pm 0.19$ at $L_{\text{FIR}} = 10^9 - 10^{12} L_{\odot}$ (Condon et al. 1990, 1991a). If, besides starburst activity, SMBH-driven activity (both radio-loud and -quiet cases) contributes strongly to the bolometric luminosity of a galaxy, strong radio synchrotron emission is expected to exist. Since this radio emission is presumably not directly coupled with far-infrared emission, the q -value is expected to be decreased. Actually, not only radio-loud AGNs but also many radio-quiet Seyfert galaxies show q -values smaller than those of starburst galaxies (Knapp et al. 1990; Elvis et al. 1994; Dahari & De Robertis 1988). Given that the rest of radio-quiet Seyfert galaxies show q -values similar to or larger than those of starburst galaxies, the q -value may not be a very sensitive indicator for the presence of SMBH-driven activity, that is, the decrease of the q -values may be recognized only when the contribution of SMBH-driven activity relative to starburst activity is high. Therefore, if the q -value of a galaxy is clearly smaller than those of starburst galaxies, we can claim with some assurance that the galaxy is strongly powered by SMBH-driven activity.

At the highest far-infrared luminosity range, the mean of q -value increases slightly, and no starburst galaxies with $L_{\text{FIR}} > 10^{11.25} L_{\odot}$ show q -values smaller than 2.05 (Condon et al. 1991b; we plot the q -value distribution of starburst galaxies with $L_{\text{FIR}} > 10^{11.25} L_{\odot}$ in the upper panel of Fig. 3). We selected four multinuclei merging IRLGs with $q < 2.0$ as candidates strongly powered by SMBH-driven activities.

The selected targets are PKS 1345+12 (= IRAS 13451+1232, 4C 12.50), Super-Antennae (= IRAS 19254–7245), IRAS 04154+1755, and Mrk 1224 (= IRAS 09018+1447, UGC 4756). Properties of these galaxies are summarized in Table 1.

PKS 1345+12 is a merging double-nuclei IRLG (Murphy et al. 1996; Surace & Sanders 1999). The q -value is -0.35 (Kim 1995). The optical spectrum is a Seyfert 2 type (Sanders et al. 1988b). Veilleux et al. (1997b) detected a broad (FWHM $\sim 2500 \text{ km s}^{-1}$) near-infrared Pa α emission line, whose intrinsic luminosity is as high as optically selected quasars.

Super-Antennae is a merging double-nuclei IRLG (Mirabel, Lutz, & Maza 1991; Duc, Mirabel, & Maza 1997). It shows an excess of radio (4.9 GHz = 6 cm) to far-infrared luminosity ratio compared to starburst galaxies (Roy & Norris 1997). Assuming a radio spectrum of ν^{-1} , we find a $q = 1.31$. The optical spectrum is a Seyfert 2 type (Mirabel et al. 1991; Duc et al. 1997). Mid-infrared observation of the $7.7 \mu\text{m}$ polycyclic aromatic hydrocarbon emission to $7.7 \mu\text{m}$ continuum luminosity ratio suggested that SMBH-driven activity contributes strongly to the bolometric luminosity (Genzel et al. 1998).

IRAS 04154+1755 has a q -value of 1.93, a Seyfert 2 type optical spectrum, and a one-sided radio jet structure (Crawford et al. 1996). In the Digitized Sky Survey image, IRAS 04154+1755 seems to be a merging system of two galaxies. We obtained near-infrared J- and K'-band images of IRAS 04154+1755 using QUIST at the University of Hawaii 0.6m telescope (Hodapp, Hora, & Metzger 1997). The image also shows two nuclei that may be interacting each other.

Mrk 1224 is a merging multinuclei IRLG (Smith et al. 1996). The q -value is 1.97, and two radio sources, which correspond to the two brightest nuclei of these galaxies, are seen (Crawford et al. 1996). The optical spectral classification is unknown.

3. Observation and Data Analysis

PKS 1345+12, Super-Antennae, IRAS 04154+1755, and Mrk 1224 were observed with the Advanced Satellite for Cosmology and Astrophysics (*ASCA*; Tanaka, Inoue, & Holt

1994). The observing log is summarized in Table 2. The observations were performed with the two solid-state imaging spectrometers (SIS0 and SIS1) and the two gas imaging spectrometers (GIS2 and GIS3). We removed data obtained under high-background environments, and used only high- and medium-bit data. The remaining effective exposure time after this data selection and net source counts are also summarized in Table 2.

Standard calibration and data reduction techniques were employed using FTOOLS software provided by the *ASCA* Guest Observer Facility. The separation of the nuclei for these sources is in the range $2''$ – $20''$, which is far smaller than the spatial resolution of *ASCA* ($2'$ for 50% encircled energy). Hence, the hard X-ray luminosities derived from *ASCA* are the sum of the emission from the nuclei of each source.

Significant X-ray photons were detected at the position of PKS 1345+12 and Super-Antennae in the SIS and GIS detectors. We extracted X-ray spectra from circular regions centered on the source with radii $2'.6$ and $3'.3$ for the SIS and GIS data of PKS 1345+12, and $2'.1$ and $3'.4$ for the SIS and GIS data of Super-Antennae, respectively. We extracted background spectra from an annular region outside the source region.

For IRAS 04154+1755 data, we marginally detected a source only in the SIS1 image. Because of the position coincidence with the radio position (Crawford et al. 1996) within the absolute pointing accuracy of *ASCA* ($\sim 1'$), we conclude this source is IRAS 04154+1755. We extracted X-ray spectra from circles of radius $2'.1$ centered on the source. For detectors other than the SIS1, we found no source candidates. For these detectors, we estimated the flux around the coordinate where a source was detected in the SIS1 image. We accumulated the X-ray photons with radii of $2'.1$ and $3'.4$ for the SIS0 and GIS detectors, respectively. Background subtraction was done in the same way as before.

For Mrk 1224 data, we identified a source candidate in the SIS0 and SIS1 images. Because of the position coincidence with the radio position (Crawford et al. 1996) within the absolute pointing accuracy of *ASCA*, we conclude this source is Mrk 1224. We extracted X-ray spectra from circles of radius $1'.6$ centered on the source. For the GIS detectors, we found no source candidates. For them, we estimated the flux around the coordinate where a source was detected in the SIS images. We accumulated the X-ray photons with a radius $3'.4$ for the GIS detectors. Background subtraction was done in the same way as before.

4. Results

4.1. PKS 1345+12

The SIS and GIS spectra of PKS 1345+12 are shown in Figures 1a and 1b, respectively. For clarity, we show the SIS and GIS data separately.

The Galactic absorption toward this source is interpolated to be $N_{\text{H}} = 1.9 \times 10^{20} \text{ cm}^{-2}$ from the Einstein On-Line Service (EINLINE; 131.142.11.73). Since this absorption is negligible for 2–10 keV band, we neglect it for the following spectral fitting. We first fit the data with a single power-law model modified by cold absorption at the rest frame ($z = 0.121$). We fit the combined SIS and GIS spectra simultaneously. The fitting results are summarized in Table 3, and are plotted in Figures 1a and 1b. The extinction-corrected hard X-ray luminosity is $L_{\text{X}} = 3.2 \times 10^{43} \text{ ergs s}^{-1}$, which corresponds to $L_{\text{X}}/L_{\text{FIR}} = 8.5 \times 10^{-3}$ ($= 10^{-2.07}$).

The derived photon index ($\Gamma = 0.82_{-0.03}^{+0.07}$) is smaller than that for typical AGNs ($\Gamma \sim 1.7$). This might be intrinsic, but such a small Γ can be reproduced if we fit poor S/N data whose intrinsic spectra are a highly absorbed power-law of $\Gamma = 1.7$. For comparison, we fix Γ as 1.7 and fit with single power-law model modified by cold absorption at the rest frame. The fitted parameters are summarized in Table 3. This model is also acceptable in terms of reduced χ^2 value. The extinction-corrected hard X-ray luminosity is consistent with the above result within 10%. We adopt the value of $L_{\text{X}} = 3.2 \times 10^{43} \text{ ergs s}^{-1}$ for the discussion.

No significant iron $\text{K}\alpha$ emission line is detected near 5.7 keV ($= 6.4 \text{ keV}/1.121$), with the equivalent width of $<466 \text{ eV}$ at the 90% confidence level. This value is smaller than those whose direct hard X-ray emission is completely blocked and for which only a scattered component is seen (equivalent width $>1 \text{ keV}$; Koyama et al. 1989; Iwasawa et al. 1993; Iwasawa & Comastri 1998; Maiolino et al. 1998; Matt et al. 1996), suggesting that the observed hard X-ray emission is not a scattered component.

The detection of broad near-infrared $\text{Pa}\alpha$ emission toward this source by Veilleux et al. (1997b) suggests this is a less obscured system by dust. Hard X-ray absorption is caused mainly by gas, while near-infrared extinction is caused by dust. If the gas-to-dust ratio toward this source was far higher than usual Galactic value ($N_{\text{H}}/A_{\text{V}} = 1.8 \times 10^{21} \text{ mag}^{-1} \text{ cm}^{-2}$; Predehl & Schmitt 1995), direct hard X-ray emission could be completely blocked even toward a source less obscured by dust. However, the hard X-ray spectra of sources with detected broad near-infrared lines (NGC 2992, MCG –05-23-16, IRAS F20460+1925, IRAS F23060+0505; Veilleux et al. 1997a, b), all of which are of higher quality than that of PKS 1345+12, show small X-ray absorption ($N_{\text{H}} < 10^{23} \text{ cm}^{-2}$; Turner et al. 1997; Ogasaka et al. 1997; Brandt et al. 1997). Therefore, we believe we see direct hard X-ray emission from SMBH-driven activity in PKS 1345+12.

4.2. Super-Antennae

The SIS and GIS spectra of Super-Antennae are shown in Figures 2a and 2b, respectively.

We fit the data with a single power-law model modified by cold absorption at the rest frame ($z = 0.062$). We fit the combined SIS and GIS spectra simultaneously. Since the expected N_{H} at the Galactic latitude of this source (-29°) is negligible for 2–10 keV band ($N_{\text{H}} = 0\text{--}2 \times 10^{21} \text{ cm}^{-2}$; Dickey and Lockman 1990), we do not include the Galactic absorption for the spectral fitting. The fitting results are summarized in Table 3, and are plotted in Figures 2a and 2b. The extinction-corrected hard X-ray luminosity is $L_{\text{X}} = 1.4 \times 10^{42} \text{ ergs s}^{-1}$, which corresponds to $L_{\text{X}}/L_{\text{FIR}} = 5.3 \times 10^{-4} (= 10^{-3.28})$.

The derived photon index ($\Gamma = 1.1_{-0.2}^{+0.1}$) is smaller than that for typical AGNs ($\Gamma \sim 1.7$). For comparison, we fix Γ as 1.7 and fit with single power-law model modified by cold absorption at the rest frame, as described in § 4.1. The fitted parameters are summarized in Table 3. This model is also acceptable in terms of reduced χ^2 value. The extinction-corrected hard X-ray luminosity is consistent with the above result within 20%.

The equivalent width of the iron $K\alpha$ emission line at 6.0 keV ($= 6.4 \text{ keV}/1.062$) is $<1630 \text{ eV}$ at the 90% confidence level. Because the upper limit of the equivalent width is large, we cannot rule out the possibility that the detected hard X-ray emission is a scattered component. If this is the case, the intrinsic hard X-ray luminosity could be much higher than the above value, and we must know the scattering efficiency to estimate intrinsic hard X-ray luminosity. To estimate the scattering efficiency, we must detect direct emission from SMBH-driven activities, which could be visible at higher energy ($>10 \text{ keV}$). The hard X-ray scattering efficiency (f_{scatt}) is estimated to be $\sim 3\%$ for the nearby Seyfert 2 galaxy, NGC 4945, which is the only object known so far whose 2–10 keV hard X-ray emission is completely blocked ($N_{\text{H}} > 10^{24} \text{ cm}^{-2}$) and whose scattering efficiency is estimated based on the direct emission detected at $>10 \text{ keV}$ (Iwasawa et al. 1993). Though its far-infrared luminosity ($L_{\text{FIR}} = 10^{10.74} L_{\odot}$) is not as high as IRLGs ($L_{\text{FIR}} > 10^{11.25} L_{\odot}$), intense far-infrared emission from the compact, dusty central region of the galaxy (Rice et al. 1988) and the coexistence of SMBH-driven and starburst activities (Moorwood & Oliva 1994) suggest that NGC 4945 has similar nuclear environment to merging IRLGs. We tentatively adopt the value of 3% as a representative value of hard X-ray scattering efficiency in merging IRLGs.

If we assume a power-law spectrum of $\Gamma = 1.7$ and a scattering efficiency of 3%, then the intrinsic hard X-ray luminosity is $2.9 \times 10^{43} \times (0.03/f_{\text{scatt}}) \text{ ergs s}^{-1}$, or $L_{\text{X}}/L_{\text{FIR}} = 1.1 \times 10^{-2} (= 10^{-1.97}) \times (0.03/f_{\text{scatt}})$.

4.3. IRAS 04154+1755

A source was detected in the SIS1 detector at a 4.8σ level, but not in the other detectors ($< 2 \sigma$). Hence, it is impossible to obtain any useful spectral information. By neglecting the small Galactic absorption ($N_{\text{H}} = 1.8 \times 10^{21} \text{ cm}^{-2}$; EINLINE), we estimate the upper limit of the hard X-ray flux at the 90% confidence level by using the combined SIS and GIS data.

We assume (1) a power-law spectrum of $\Gamma = 1.0$, as observed for PKS 1345+12 and Super-Antennae, (2) a power-law spectrum of $\Gamma = 1.7$ modified by cold absorption with $N_{\text{H}} = 10^{23} \text{ cm}^{-2}$ at the rest frame ($z = 0.056$), and (3) that direct hard X-ray emission is completely blocked ($N_{\text{H}} > 10^{24} \text{ cm}^{-2}$) and only a scattered component ($\Gamma = 1.7$) is seen with a scattering efficiency of 3%. The estimated hard X-ray flux and extinction-corrected hard X-ray luminosity are summarized in Table 3.

4.4. Mrk 1224

A source was detected in the SIS detectors, but the detection was only $\sim 5 \sigma$ (SIS0) and $\sim 3 \sigma$ (SIS1). For the GIS detectors, source detection was $< 3 \sigma$ for each. It is therefore impossible to obtain any useful spectral information. We neglect the small Galactic absorption ($N_{\text{H}} = 3.7 \times 10^{20} \text{ cm}^{-2}$; EINLINE), and estimate the upper limit of the hard X-ray flux and extinction-corrected hard X-ray luminosity at the 90% confidence level by using the combined SIS and GIS data, as we did with the IRAS 04154+1755 data. The results are summarized in Table 3.

5. Discussion

5.1. Hard X-ray Luminosity Relative to Far-Infrared and Infrared Luminosity

In Table 4, we summarize the hard X-ray emission properties of the four radio-excess multinuclei merging IRLGs. For comparison, we examine the hard X-ray emission properties of AGNs (= Seyfert type optical spectra) and radio-excess multinuclei merging IRLGs in the literature. We summarize the results in Table 5. To find hard X-ray data, we first examined Turner et al. (1997) and Nandra et al. (1997) for *ASCA* data, Nandra & Pounds (1994) for *Ginga* data, and Elvis et al. (1994) for *HEAO1* data. We include additional sources for which hard X-ray data are available in other papers. If a source was observed both with *Ginga* and *ASCA*, we adopt the *ASCA* data, but show the *Ginga* data

for comparison in Table 5. This is because time variation of the hard X-ray luminosity from SMBH-driven activity is sometimes significant. In our sample, NGC 2992 and Mrk 3 show time variations of a factor of >4 . We then examined the far-infrared and radio 1.5 GHz data for these AGNs. If radio data were taken at different epochs, we adopted the latest data, though the differences were always less than a factor of 1.8, corresponding to $\Delta q < 0.25$. In some cases, we estimated radio 1.5 GHz flux from measurements at other radio frequencies near 1.5 GHz (1.4, 2.3, and 4.8 GHz). In Table 5, we compile all AGNs for which an intrinsic hard X-ray luminosity has been derived, and far-infrared and radio data are available. However, we do not include the objects whose hard X-ray emission is convincingly a scattered component based both on a large equivalent width of the iron $K\alpha$ emission line and on the spectral shape in the hard X-ray band, where the intrinsic hard X-ray luminosity is highly uncertain. These are NGC 1068 (Koyama et al. 1989), NGC 4388 (Netzer, Turner, & George 1998), NGC 7674 (Malaguti et al. 1998), and NGC 6240 (Nakagawa et al. 1997; Iwasawa & Comastri 1998). We do not include flat spectrum compact-radio sources in Elvis et al. (1994; 3C273, Q0007+106, Q1028+313, Q1721+343), because their hard X-ray emission could be relativistically beamed toward our line of sight.

In Figure 3, we plot L_X/L_{FIR} ratios of multinuclei merging IRLGs and AGNs against observed q -values, where we add Mrk 463 to our sample of radio-excess multinuclei merging IRLGs. For radio-excess sources ($q < 2.0$), which we regard as sources strongly powered by SMBH-driven activity ³, we find a clear difference of L_X/L_{FIR} ratios between AGNs and multinuclei merging IRLGs. The L_X/L_{FIR} of radio-excess AGNs is actually high as we anticipated, but the five radio-excess multinuclei merging IRLGs (the four merging IRLGs and Mrk 463) show L_X/L_{FIR} ratios far smaller than the AGNs with a similar radio-excess. The AGN NGC 2992 shows a small L_X/L_{FIR} ($\sim 10^{-2.12}$) ratio, but the hard X-ray luminosity derived from *ASCA*, which we adopted, is about 4 times smaller than that derived from *Ginga* data. Hence, the *ASCA* observation of NGC 2992 may have been made during a very faint phase. All the radio-excess AGNs in Table 5 show single-nucleus morphology, and an *IRAS* 25 μm to 60 μm flux ratio of $\gtrsim 0.2$ (i.e., “warm color”; Sanders et al. 1988b), indicating they are in the later or final stage of merging. This suggests that, during the early stage of a merger, the L_X/L_{FIR} ratio appears to be considerably smaller than that in the later or final stage, even though a similar radio-excess is found.

Most of multinuclei merging IRLGs show a spectral energy distribution that peaks at 60 μm and radiates a predominant fraction of infrared (8– 1000 μm) emission in the

³ We note a galaxy can be powered by starburst activity even though the galaxy shows a Seyfert type optical spectrum (e.g., Genzel et al. 1995). For $q > 2.0$ AGNs, we have no strong evidence that they are powered by SMBH-activity. Actually, the L_X/L_{FIR} ratios distribute from 10^{-4} to 10^0 in Figure 3.

far-infrared (40–500 μm), while many ordinary AGNs do not. This different spectral energy distribution in the infrared region could cause the difference in the L_X/L_{FIR} ratios in Figure 3. We compare the extinction-corrected hard X-ray luminosities with infrared luminosities (L_{IR}). The L_X/L_{IR} ratios plotted against observed q -values ($\equiv \log f_{\text{IR}}/f_{20\text{cm}}$) are shown in Figure 4. The radio-excess multinuclei merging IRLGs still show L_X/L_{IR} ratios smaller by a large factor than those of AGNs with a similar radio-excess.

5.2. Possible Explanations and Implications

We consider four possible explanations for the small L_X/L_{FIR} and L_X/L_{IR} ratios in radio-excess multinuclei merging IRLGs compared with radio-excess AGNs. (1) A high fraction of UV to soft X-ray emission is absorbed by dust in the multinuclei merging IRLGs, (2) direct hard X-ray emission suffers partial absorption in the multinuclei merging IRLGs, (3) direct hard X-ray emission is completely blocked, and nearly no scattered component is seen in the multinuclei merging IRLGs, and (4) emission in the hard X-ray region from SMBH-driven activity in the multinuclei merging IRLGs is severely suppressed compared to a typical spectral energy distribution of SMBH-driven activity in AGNs. We will consider each explanation below and suggest that the fourth one is the most plausible to us.

Let us consider the first explanation. If the fraction of UV to soft X-ray emission from SMBH-driven activity absorbed by dust and reradiated in the infrared is high in the multinuclei merging IRLGs, the L_{IR} will increase, and thus L_X/L_{IR} will become apparently smaller. Since a mass concentration of molecular gas toward the nuclei is found in some IRLGs (Scoville, Yun & Bryant 1997, Bryant & Scoville 1996), the high fraction is quite possible. However, the fraction of UV to soft X-ray emission absorbed by dust and reradiated in the infrared region in AGNs is $\sim 30\text{--}50\%$ (Sanders et al. 1989; Rowan-Robinson 1995). Even if we consider nearly 100% of UV to soft X-ray emission from SMBH-driven activity is absorbed by dust in the multinuclei merging IRLGs, the L_X/L_{IR} could decrease by only a factor of 2–3. Hence, this explanation alone cannot explain the observed large difference.

Next, we consider the second explanation that the hard X-ray emission suffers partial absorption by X-ray absorbing gas such that a large fraction of the X-ray emission is completely blocked but the remaining small fraction is relatively transparent. If this is the case, we cannot estimate correctly the hard X-ray extinction from the observed hard X-ray spectra, and thus the intrinsic hard X-ray luminosity could be higher than the derived extinction-corrected hard X-ray luminosity from the observed spectra. However, the intrinsic size of X-ray emission from SMBH-driven activity is considered very compact

($<10^{-3}$ pc; Barr & Mushotzky 1986). To achieve partial absorption, the size of the clumps of the absorbing gas must be far smaller than 10^{-3} pc, and yet each clump must have column density higher than $N_{\text{H}} > 10^{24} \text{ cm}^{-2}$.

We then consider the third explanation that direct hard X-ray emission is completely blocked and nearly no scattered component is seen. However, the detection of near-infrared broad emission lines toward PKS 1345+12 and Mrk 463 (Veilleux et al. 1997a,b) indicates we detect direct hard X-ray emission from SMBH-driven activity in these sources, as discussed in § 4.1. For other three sources, Super-Antennae, IRAS 04154+1755, and Mrk 1224, the detection of broad optical or near-infrared emission lines has not been reported. If a direct component is completely blocked and nearly no scattered component is seen ($f_{\text{scatt}} < 0.5\%$), intrinsic $L_{\text{X}}/L_{\text{IR}}$ ratios could be in the range of AGNs. Super-Antennae and IRAS 04154+1755 show Seyfert 2 type optical spectra. This suggests a large amount of ionizing UV to soft X-ray photons from SMBH-driven activity are escaping in directions roughly perpendicular to our line of sight (i.e., the SMBH-driven activity is *not* completely obscured toward *all* directions). We expect the scattering efficiency is high in the multinuclei merging IRLGs, since plenty of scattering material is thought to exist in the vicinity of SMBHs. Hence, the very small scattering efficiency appears not to be natural for these sources. Future high-quality data at >10 keV could be used to see whether direct hard X-ray emission is toward us or not, and, in the latter case, to estimate the scattering efficiency.

We consider the result suggests that emission in the hard X-ray region from SMBH-driven activity in the multinuclei merging IRLGs is severely suppressed compared to a typical spectral energy distribution of SMBH-activity in AGNs. For all five radio-excess multinuclei merging IRLGs, the presence of strong synchrotron radio emission from SMBH-driven activity is suggested. The presence of strong UV to soft X-ray emission from SMBH-driven activity, which can account for a predominant fraction of their huge bolometric luminosity (Veilleux et al. 1997b; Genzel et al. 1998), is also suggested in PKS 1345+12, Mrk 463, and Super-Antennae. These sources are supposed to have strong SMBH-driven activity, perhaps through a high mass accretion rate onto an SMBH, and yet hard X-ray luminosity is small. The hard X-ray emission mechanism in the vicinity of an SMBH is thought to be through inverse Compton upscattering of UV to soft X-ray photons by high energetic electrons in a hot corona (e.g., Walter & Courvoisier 1992). It may be that, in merging IRLGs, these high energy electrons are not produced as much as in AGNs, or lose energy in a short time scale.

In the high-redshift universe, the global (rest-frame) far-infrared emission is dominated by merging IRLGs (Sanders 1999). Hence, the energy source of merging IRLGs is directly coupled with the global interplay between starburst and SMBH-driven activity. The energy

source of these high-redshift merging IRLGs will be investigated using the next generation of high-sensitivity hard X-ray satellites. However, if the suppression of hard X-ray emission suggested from the study of nearby merging IRLGs is applicable also to high-redshift merging IRLGs, without its correction, hard X-ray observations would underestimate the contribution of SMBH-driven activity in high-redshift merging IRLGs. We should understand the hard X-ray emission properties from SMBH-driven activity in nearby AGNs and merging IRLGs.

6. Summary

We found the following main results:

1. The hard X-ray luminosities relative to far-infrared and infrared luminosities in the radio-excess multinuclei merging IRLGs are considerably smaller than those in radio-excess AGNs.
2. This result may show that emission in the hard X-ray region from SMBH activity in the multinuclei merging IRLGs is severely suppressed compared to a typical spectral energy distribution of SMBH-driven activity in AGNs.
3. If this is generally applicable to merging IRLGs, without its correction, hard X-ray observations underestimate the contribution of SMBH-driven activity to the bolometric luminosities of merging IRLGs.

We thank all of the members of the *ASCA* team who made this study possible. We thank Dr. C. C. Dudley and Ms. L. Good for their careful reading of the manuscript, Dr. H. Awaki for a useful discussion, and Dr. N. Kobayashi for giving us part of his QUIST observing time. We are grateful to the anonymous referee for useful comments. MI and SU are financially supported by the Japan Society for the Promotion of Science for their stays at the University of Hawaii and the University of Leicester, respectively. The Galactic absorption data were obtained from the Einstein On-Line Service, Smithsonian Astrophysical Observatory (EINLINE). This research was supported by a Grant-in-Aid for Scientific Research on Priority Areas funded by the Ministry of Education, Science, Sports, and Culture of Japan.

REFERENCES

- Alonso-Herrero, A., Ward, M. J., & Kotilainen, J. K. 1997, MNRAS, 288, 977
- Barr, P., & Mushotzky, R. F. 1986, Nature, 320, 421
- Barvainis, R., Lonsdale, C., & Antonucci, R. 1996, AJ, 111, 1431
- Bicay, M. D., Kojoian, G., Seal, J., Dickinson, D. F., & Malkan, M. A. 1995, ApJS, 98, 369
- Brandt, W. N., Fabian, A. C., Takahashi, K., Fujimoto, R., Yamashita, A., Inoue, H., & Ogasaka, Y. 1997, MNRAS, 290, 617
- Bransford, M. A., Appleton, P. N., Heisler, C. A., Norris, R. P., & Marston, A. P. 1998, ApJ, 497, 133
- Bryant, P. M., & Scoville, N. Z. 1996, ApJ, 457, 678
- Condon, J. J. 1987, ApJS, 65, 485
- Condon, J. J., Anderson, M. L., & Helou, G. 1991a, ApJ, 376, 95
- Condon, J. J., Helou, G., Sanders, D. B., & Soifer, B. T. 1990, ApJS, 73, 359
- Condon, J. J., Huang, Z. -P., Yin, Q. F., & Thuan, T. X. 1991b, ApJ, 378, 65
- Crawford, T., Marr, J., Partridge, B., & Strauss, M. A. 1996, ApJ, 460, 225
- Dahari, O., & De Robertis, M. M. 1988, ApJS, 67, 249
- Dickey, J. M., & Lockman, F. J. 1990, ARA&A, 28, 215
- Duc, P. -A., Mirabel, I. F., & Maza, J. 1997, A&AS, 124, 533
- Elvis, M., Wilkes, B. J., McDowell, J. C., Green, R. F., Bechtold, J., Willner, S. P., Oey, M. S., Polonski, E., & Cutri, R. 1994, ApJS, 95, 1
- Genzel, R., Weitzel, L., Tacconi-Garman, L. E., Blietz, M., Cameron, M., Krabbe, A., and Lutz, D., 1995, ApJ, 444, 129
- Genzel, R., et al. 1998, ApJ, 498, 579
- Griffiths, R. G., Warwick, R. S., Georgantopoulos, I., Done, C., & Smith, D. A. 1998, MNRAS, 298, 1159
- Harnett, J. I. 1987, MNRAS, 227, 887

- Heisler, C. A., Norris, R. P., Jauncey, D. L., Reynolds, J. E., & King, E. A. 1998, MNRAS, 300, 1111
- Helou, G., Soifer, B. T., & Rowan-Robinson, M. 1985, ApJ, 298, L7
- Hodapp, K. -W., Hora, J. L., & Metzger, M. R. 1997, Observer’s Guide for QUIRC, <http://www.ifa.hawaii.edu/88inch/>
- Hutchings, J. B., & Neff, S. G. 1991, AJ, 101, 434
- Imanishi, M., & Ueno, S. 1999, MNRAS, 305, 829
- Iwasawa, K. 1999, MNRAS, 302, 96
- Iwasawa, K., & Comastri, A. 1998, MNRAS, 297, 1219
- Iwasawa, K., Koyama, K., Awaki, H., Kunieda, H., Makishima, K., Tsuru, T., Ohashi, T., & Nakai, N. 1993, ApJ, 409, 155
- Kim, D. -C. 1995, Ph.D. thesis, University of Hawaii
- Knapp, G. R., Bies, W. E., & van Gorkom, J. H. 1990, AJ, 99, 476
- Koyama, K., Inoue, H., Tanaka, Y., Awaki, H., Takano, S., Ohashi, T., & Matsuoka, M. 1989, PASJ, 41, 731
- Lutz, D., Veilleux, S., & Genzel, R. 1999, astro-ph/9903152
- Maiolino, R., Salvati, M., Bassani, L., Dadina, M., Della Ceca, R., Matt, G., Risaliti, G., & Zamorani, G. 1998, A&A, 338, 781
- Malaguti, G., et al. 1998, A&A, 331, 519
- Matt, G., et al. 1996, MNRAS, 281, L69
- Mirabel, I. F., Lutz, D., & Maza, J. 1991, A&A, 243, 367
- Moorwood, A. F., & Oliva, E. 1994, ApJ, 429, 602
- Murphy, T. W., Jr., Armus, L., Matthews, K., Soifer, B. T., Mazzarella, J. M., Shupe, D. L., Strauss, M. A., & Neugebauer, G. 1996, AJ, 111, 1025
- Nagar, N. M., Wilson, A. S., Mulchaey, J. S., & Gallimore, J. F. 1999, ApJS, 120, 209

- Nakagawa, T., Kii, T., Fujimoto, R., Miyazaki, T., Inoue, H., Ogasaka, Y., Arnaud, K., & Kawabe, R. 1997, in IAU Symp, 186, Galaxy Interactions at Low and High Redshift, p.103
- Nandra, K., & Pounds, K. A. 1994, MNRAS, 268, 405
- Nandra, K., George, I. M., Mushotzky, R. F., Turner, T. J., & Yaqoob, T. 1997, ApJ, 477, 602
- Netzer, H., Turner, T. J., & George, I. M. 1998, ApJ, 504, 680
- Ogasaka, Y., Inoue, H., Brandt, W. N., Fabian, A. C., Kii, T., Nakagawa, T., Fujimoto, R., & Otani, C. 1997, PASJ, 49, 179
- Predehl P., & Schmitt J. H. M. M. 1995, A&A, 293, 889
- Rice, W., Lonsdale, C. L., Soifer, B. T., Neugebauer, G., Kopan, E. L., Lloyd, L. A., De Jong, T., & Habing, H. J. 1988, ApJS, 68, 91
- Rowan-Robinson, M. 1995, MNRAS, 272, 737
- Roy, A. L., & Norris, R. P. 1997, MNRAS, 289, 824
- Roy, A. L., Norris, R. P., Kesteven, M. J., Troup, E. R., & Reynolds, J. E. 1994, ApJ, 432, 496
- Rush, B., Malkan, M. A., & Edelson, R. A. 1996, ApJ, 473, 130
- Sanders, D. B., 1999, astro-ph/9904292
- Sanders, D. B., & Mirabel, I. F. 1996, ARA&A, 34, 749
- Sanders, D. B., Phinney, E. S., Neugebauer, G., Soifer, B. T., & Matthews, K. 1989, ApJ, 347, 29
- Sanders, D. B., Soifer, B. T., Elias, J. H., Madore, B. F., Matthews, K., Neugebauer, G., & Scoville, N. Z. 1988a, ApJ, 325, 74
- Sanders, D. B., Soifer, B. T., Elias, J. H., Neugebauer, G., & Matthews, K. 1988b, ApJ, 328, L35
- Scoville, N. Z., Yun, M. S., & Bryant, P. M. 1997, ApJ, 484, 702
- Smith, D. A., Herter, T., Haynes, M. A., Beichman, C. A., & Gautier, T. N., III 1996, ApJS, 104, 217

- Surace, J. A., & Sanders, D. B. 1999, *ApJ*, 512, 162
- Tanaka, Y., Inoue, H., & Holt, S. S. 1994, *PASJ*, 46, L37
- Taniguchi, Y., Yoshino, A., Ohyama, Y., & Nishiura, S. 1999, *ApJ*, 514, 660
- Tsuru, T. 1992, Ph.D. thesis, University of Tokyo
- Turner, T. J., George, I. M., Nandra, K., & Mushotzky, R. F. 1997, *ApJ*, 488, 164
- Ueno, S., Koyama, K., Awaki, H., Hayashi, I., & Blanco, P. R. 1996, *PASJ*, 48, 389
- Ulvestad, J. S., & Wilson, A. S. 1984, *ApJ*, 285, 439
- Veilleux, S., Kim, D. -C., Sanders, D. B., Mazzarella, J. M., & Soifer, B. T. 1995, *ApJS*, 98, 171
- Veilleux, A., Goodrich, R. W., & Hill, G. 1997a, *ApJ*, 477, 631
- Veilleux, S., Sanders, D. B., & Kim, D. -C. 1997b, *ApJ*, 484, 92
- Wall, J. V., & Peacock, J. A. 1985, *MNRAS*, 216, 173
- Walter, R., & Courvoisier, T. J., -L. 1992, *A&A*, 258, 255

Fig. 1.— (a): The SIS X-ray spectrum of PKS 1345+12. Open circles: SIS0 data. Filled squares: SIS1 data. The solid and dotted lines are fitted results for the SIS0 and SIS1, respectively (see text). (b): The GIS X-ray spectrum of PKS 1345+12. Open triangles: GIS2 data. Filled stars: GIS3 data. The solid and dotted lines are fitted results for the GIS2 and GIS3, respectively.

Fig. 2.— (a) and (b): The SIS and GIS X-ray spectrum of Super-Antennae, respectively. Same symbols as in Figure 1.

Fig. 3.— *Upper*: The q -value distribution of starburst galaxies at high far-infrared luminosities [$\log(L_{\text{FIR}}/L_{\odot}) \geq 11.25$]. In total, 27 sources are plotted. No starburst galaxies show $q < 2.05$. We plotted IRLGs with starburst-type and LINER-type optical spectra. We included IRLGs with LINER-type spectra (11 sources) because shock heating driven by superwind activity rather than AGN activity is thought to be responsible for their spectra (Taniguchi et al. 1999; Lutz, Veilleux, & Genzel 1999). Samples are taken from Condon et al. (1991b), and optical classifications are from Veilleux et al. (1995). *Lower*: Correlation between $L_{\text{X}}/L_{\text{FIR}}$ and observed q -values of AGNs and multinuclei merging IRLGs. Dashed line: $q = 2.0$. We regard sources with $q < 2.0$ as radio-excess sources. Open squares: $q < 2.0$ radio-excess AGNs. Filled circles: $q < 2.0$ radio-excess multinuclei merging IRLGs (PKS 1345+12, Super-Antennae, IRAS 04154+1755, Mrk 1224, and Mrk 463). Open circles: $q > 2.0$ AGNs. For Super-Antennae, IRAS 04154+1755, and Mrk 1224, we plotted the data by assuming that only a scattered component is seen and the scattering efficiency is 3%. Note that if direct hard X-ray emission is toward us, the $L_{\text{X}}/L_{\text{FIR}}$ is far smaller than the plotted positions.

Fig. 4.— *Upper*: The q' -value distribution of starburst galaxies at high far-infrared luminosities [$\log(L_{\text{FIR}}/L_{\odot}) \geq 11.25$]. The sample sources are the same as in Figure 3. No starburst galaxies show $q' < 2.1$. *Lower*: Correlation between $L_{\text{X}}/L_{\text{IR}}$ and observed q' -values. Dashed line: $q' = 2.1$. We regard sources with $q' < 2.1$ as radio-excess sources. Open squares: $q' < 2.1$ radio-excess AGNs. Filled circles: $q' < 2.1$ radio-excess multinuclei merging IRLGs. Open circles: $q' > 2.1$ AGNs.

Table 1. Summary of the Properties of the Four Radio-Excess Multinuclei Merging IRLGs

Objects (1)	z (2)	f_{12} (Jy) (3)	f_{25} (Jy) (4)	f_{60} (Jy) (5)	f_{100} (Jy) (6)	$\log L_{\text{FIR}}$ (ergs s ⁻¹) (7)	q (8)	$\log L_{\text{IR}}$ (ergs s ⁻¹) (9)	q' (10)	$\frac{f_{25}}{f_{60}}$ (11)
PKS 1345+12	0.121	0.14	0.67	1.92	2.06	45.57	-0.35 ^a	45.82	-0.10	0.35
Super-Antennae	0.062	0.22	1.24	5.48	5.79	45.43	1.31 ^b	45.60	1.48	0.23
IRAS 04154+1755	0.056	0.20	0.71	3.82	5.84	45.24	1.93 ^c	45.39	2.09	0.19
Mrk 1224	0.050	0.18	0.50	4.12	6.98	45.19	1.97 ^c	45.30	2.08	0.12

^aKim 1995.

^bRoy & Norris 1997.

^cCrawford et al. 1996.

Note. — Column (1): Object name. Column (2): Redshift. Column (3): IRAS 12 μm flux in Jy. Column (4): IRAS 25 μm flux in Jy. Column (5): IRAS 60 μm flux in Jy. Column (6): IRAS 100 μm flux in Jy. Column (7): Logarithm of far-infrared (40–500 μm) luminosity in ergs s⁻¹ calculated with $L_{\text{FIR}} = 2.1 \times 10^{39} \times D(\text{Mpc})^2 \times (2.58 \times f_{60} + f_{100})$ [ergs s⁻¹] (Sanders & Mirabel 1996). Column (8): Observed q -value. Column (9): Logarithm of infrared (8–1000 μm) luminosity in ergs s⁻¹ calculated with $L_{\text{IR}} = 2.1 \times 10^{39} \times D(\text{Mpc})^2 \times (13.48 \times f_{12} + 5.16 \times f_{25} + 2.58 \times f_{60} + f_{100})$ [ergs s⁻¹] (Sanders and Mirabel 1996). Column (10): Observed q' -value [$\equiv \log(f_{\text{IR}}/f_{20\text{cm}})$]. Column (11): IRAS 25 μm to 60 μm flux ratio.

Table 2. Observing Log

Objects	Observing Date	Integration ^a		Net Counts ^b	
		SIS	GIS	SIS	GIS
PKS 1345+12	1996 Jul 20	19	20	309 ± 21	311 ± 16
Super-Antennae	1996 Oct 16	33	37	191 ± 21	204 ± 21
IRAS 04154+1755	1998 Feb 15	31	35	82 ± 18	15 ± 20
Mrk 1224	1998 Nov 11	21	24	72 ± 14	63 ± 17

^aThe SIS and GIS exposure time in ksec, respectively.

^bNet source counts of the sum of SIS0 + SIS1 and GIS2 + GIS3, respectively. Errors are background photon noise (1σ).

Table 3. Fitting Results of the Four Radio-Excess Multinuclei Merging IRLGs

Objects (1)	Γ (2)	N_{H} (10^{21} cm^{-2}) (3)	$f_{\text{X}}(2\text{--}10 \text{ keV})$ ($\text{ergs s}^{-1} \text{ cm}^{-2}$) (4)	$L_{\text{X}}(2\text{--}10 \text{ keV})$ (ergs s^{-1}) (5)	χ^2/dof (6)
PKS 1345+12	$0.82^{+0.07}_{-0.03}$ 1.7 (fixed)	15^{+4}_{-3} 39^{+6}_{-3}	1.0×10^{-12} 8.2×10^{-13}	3.2×10^{43} 3.0×10^{43}	55.0/51 61.1/52
Super-Antennae	$1.1^{+0.1}_{-0.2}$ 1.7 (fixed) 1.7 (fixed)	<0.2 $3.1^{+3.9}_{-0.7}$ >1000 (fixed)	1.9×10^{-13} 1.5×10^{-13} 1.1×10^{-13}	1.4×10^{42} 1.2×10^{42} $2.9 \times 10^{43} \times (0.03/f_{\text{scatt}})$	35.3/51 38.0/52 39.1/53
IRAS 04154+1755	1.0 (fixed) 1.7 (fixed) 1.7 (fixed)	0.0 (fixed) 100 (fixed) >1000 (fixed)	$<9.6 \times 10^{-14}$ $<9.1 \times 10^{-14}$ $<5.5 \times 10^{-14}$	$<5.9 \times 10^{41}$ $<9.2 \times 10^{41}$ $<1.1 \times 10^{43} \times (0.03/f_{\text{scatt}})$	— — —
Mrk 1224	1.0 (fixed) 1.7 (fixed) 1.7 (fixed)	0.0 (fixed) 100 (fixed) >1000 (fixed)	$<1.7 \times 10^{-13}$ $<1.5 \times 10^{-13}$ $<1.0 \times 10^{-13}$	$<8.4 \times 10^{41}$ $<1.2 \times 10^{42}$ $<1.7 \times 10^{43} \times (0.03/f_{\text{scatt}})$	— — —

Note. — Column (1): Object name. Column (2): Power-law photon index. Errors are for the 1σ level ($\Delta\chi^2 = 1.0$ for one interesting parameter). Column (3): Column density of absorbing gas at the rest frame. Errors are for the 1σ level. Column (4): Hard X-ray flux. Column (5): Extinction-corrected hard X-ray luminosity. Column (6): Reduced χ^2 value.

Table 4. Summary of the Hard X-ray Properties of the Four Radio-Excess Multinuclei Merging IRLGs

Objects (1)	$\log L_X$ (ergs s ⁻¹) (2)	$\log \frac{L_X}{L_{\text{FIR}}}$ (3)	$\log \frac{L_X}{L_{\text{IR}}}$ (4)
PKS 1345+12	43.50	-2.07	-2.32
Super-Antennae	42.15 (43.46)	-3.28 (-1.97)	-3.45 (-2.14)
IRAS 04154+1755	<41.96 (<43.04)	< -3.28 (< -2.20)	< -3.43 (< -2.35)
Mrk 1224	<42.08 (<43.23)	< -3.11 (< -1.96)	< -3.22 (< -2.07)

Note. — Column (1): Object name. Column (2): Logarithm of extinction-corrected hard X-ray luminosity. Column (3): Logarithm of hard X-ray to far-infrared luminosity ratio. Column (4): Logarithm of hard X-ray to infrared luminosity ratio. Values in parentheses are for the case when only a scattered component is seen and the scattering efficiency is 3%.

Table 5. Summary of the Properties of AGNs and Radio-Excess Merging IRLGs in the Literature

Objects (1)	z (2)	$\log L_X$ (ergs s ⁻¹) (3)	$\log L_{\text{FIR}}$ (ergs s ⁻¹) (4)	$\log \frac{L_X}{L_{\text{FIR}}}$ (5)	q (6)	$\log L_{\text{IR}}$ (ergs s ⁻¹) (7)	$\log \frac{L_X}{L_{\text{IR}}}$ (8)	q' (9)	$\frac{f_{25}}{f_{60}}$ (10)	Class (11)
$q < 2.0$ radio-excess multinuclei merging IRLGs										
Mrk 463	0.050	42.40 ^a	44.82	-2.42	0.83 ^j	45.32	-2.92	1.33	0.74	N
$q < 2.0$ radio-excess AGNs										
Mrk 937	0.030	42.53 ^a	43.91	-1.38	>1.60 ^{k,1}	44.26	-1.73	>1.95	0.46	N
NGC 526A	0.019	43.42 ^a (42.83 ^b)	43.26	0.16	1.67 ^l	43.99	-0.57	2.40	2.0	N
NGC 2110	0.008	42.47 ^a (42.50 ^b)	43.55	-1.08	1.32 ^l	43.73	-1.26	1.50	0.20	N
NGC 2992	0.008	41.70 ^a (42.31 ^b)	43.82	-2.12	1.71 ^m	43.98	-2.28	1.87	0.20	N
NGC 4968	0.010	42.10 ^a	43.51	-1.41	1.93 ^j	43.86	-1.76	2.28	0.53	N
IC 5063	0.011	42.80 ^a	43.94	-1.14	0.76 ^{n,2}	44.39	-1.59	1.21	0.64	N
Mrk 335	0.025	43.07 ^c (43.24 ^b)	43.50	-0.43	1.86 ^l	44.21	-1.14	2.57	1.1	B
3C 120	0.033	43.99 ^c	44.36	-0.37	-0.33 ^j	44.73	-0.74	0.04	0.54	B
IC 4329A	0.016	43.59 ^c (43.83 ^b)	43.78	-0.19	1.59 ^l	44.46	-0.87	2.27	1.1	B
NGC 5548	0.017	43.41 ^c (43.31 ^b)	43.64	-0.23	1.81 ^l	44.12	-0.71	2.29	0.73	B
NGC 5506	0.006	42.73 ^b	43.60	-0.87	1.60 ^j	43.93	-1.20	1.93	0.41	N
3C 390.3	0.056	44.46 ^b	44.10	0.36	-0.54 ^{o,3}	44.68	-0.22	0.04	1.4	B
NGC 7213	0.006	42.43 ^b	43.27	-0.84	1.48 ^{n,4}	43.53	-1.10	1.74	0.29	B
Q0637-752	0.651	45.79 ^d	<46.22	> -0.43	< -1.21 ^{d,3}	<46.67	> -0.88	< -0.76	0.65	B
Q0837-120	0.198	44.69 ^d	<44.53	>0.16	< -0.29 ^{d,3}	<45.12	> -0.43	<0.30	<0.70	B
Mrk 279	0.031	43.38 ^d	44.23	-0.85	1.88 ^d	<44.52	> -1.14	<2.17	0.24	B
Q2135-147	0.200	44.91 ^d	<45.16	> -0.25	<0.57 ^d	<45.68	> -0.77	<1.09	0.82	B
Mrk 3	0.014	42.66 ^{e,5} (43.33 ^e)	43.93	-1.27	0.63 ^l	44.38	-1.72	1.08	0.73	N
Mrk 348	0.015	43.02 ^{f,6}	43.63	-0.61	0.79 ^l	44.03	-1.01	1.19	0.53	N
$q > 2.0$ AGNs										
NGC 1667	0.015	40.11 ^a	44.37	-4.26	2.32 ^p	44.49	-4.38	2.44	0.11	N
NGC 1808	0.003	40.27 ^a	44.16	-3.89	2.40 ^q	44.29	-4.02	2.53	0.16	N
NGC 4507	0.012	41.93 ^a	43.92	-1.99	2.21 ^{n,2}	44.17	-2.24	2.46	0.31	N
NGC 5135	0.014	42.81 ^a	44.67	-1.86	2.10 ^j	44.79	-1.98	2.22	0.15	N
ESO 103-G35	0.013	42.79 ^a	43.63	-0.84	2.29 ^{r,2}	44.22	-1.43	2.88	1.04	N
NGC 7172	0.009	42.87 ^a (42.69 ^b)	43.85	-0.98	2.50 ^j	43.99	-1.12	2.64	0.13	N
NGC 7314	0.005	42.24 ^a (42.29 ^b)	43.25	-1.01	2.37 ^q	43.36	-1.12	2.48	0.15	N
NGC 7582	0.005	41.97 ^a	44.27	-2.30	2.39 ^q	44.38	-2.41	2.50	0.13	N
NGC 3227	0.003	41.66 ^c (42.10 ^b)	43.07	-1.41	2.10 ^j	43.24	-1.58	2.27	0.22	B

Table 5—Continued

Objects (1)	z (2)	$\log L_X$ (ergs s $^{-1}$) (3)	$\log L_{\text{FIR}}$ (ergs s $^{-1}$) (4)	$\log \frac{L_X}{L_{\text{FIR}}}$ (5)	q (6)	$\log L_{\text{IR}}$ (ergs s $^{-1}$) (7)	$\log \frac{L_X}{L_{\text{IR}}}$ (8)	q' (9)	$\frac{f_{25}}{f_{60}}$ (10)	Class (11)
NGC 3516	0.009	43.08 ^c (42.54 ^b)	43.26	−0.18	2.38 ^l	43.69	−0.61	2.81	0.53	B
NGC 3783	0.009	42.90 ^c (43.05 ^b)	43.58	−0.68	>2.78 ^{s,2}	44.01	−1.11	>3.21	0.72	B
NGC 4051	0.002	41.21 ^c (41.13 ^b)	42.76	−1.55	2.54 ^j	42.92	−1.71	2.70	0.17	B
Mrk 766	0.012	42.73 ^c	43.86	−1.13	2.10 ^l	44.13	−1.40	2.37	0.34	B
NGC 4593	0.009	42.71 ^c (42.69 ^b)	43.56	−0.85	3.33 ^t	43.80	−1.09	3.57	0.33	B
MCG−6-30-15	0.008	42.72 ^c (42.83 ^b)	42.93	−0.21	2.89 ^m	43.46	−0.74	3.42	0.74	B
Mrk 841	0.036	43.47 ^c (43.33 ^b)	43.91	−0.44	>2.00 ^m	44.49	−1.02	>2.58	1.0	B
NGC 6814	0.006	40.93 ^c	43.61	−2.68	3.27 ^m	43.70	−2.77	3.36	0.10	B
Mrk 509	0.035	44.03 ^c (44.10 ^b)	44.34	−0.31	2.12 ^m	44.76	−0.73	2.54	0.52	B
NGC 7469	0.017	43.25 ^c (43.31 ^b)	45.02	−1.77	2.31 ^j	45.18	−1.93	2.47	0.20	B
Akn 120	0.033	43.88 ^b	44.01	−0.13	2.06 ^u	44.54	−0.66	2.59	0.64	B
Mrk 705	0.028	43.25 ^d	43.87	−0.62	>2.69 ^d	44.24	−0.99	>3.06	0.47	B
Q2130+099	0.061	43.57 ^d	44.28	−0.71	2.02 ^d	44.85	−1.28	2.59	0.66	B
Mrk 231	0.042	42.34 ^g	45.86	−3.52	2.22 ^v	46.06	−3.72	2.42	0.25	B/U
IRAS F20460+1925	0.181	44.08 ^h	45.52	−1.44	2.18 ^{r,2}	46.02	−1.94	2.68	0.65	N/U
IRAS F23060+0505	0.174	44.18 ⁱ	45.63	−1.45	>2.62 ^{r,2}	45.99	−1.81	>2.98	0.37	N/U

Note. — Column (1): Object name. Column (2): Redshift. Column (3): Logarithm of extinction-corrected hard X-ray luminosity. If both the *ASCA* and *Ginga* data are available, we have adopted *ASCA* data and showed *Ginga* data for comparison in parentheses. Column (4): Logarithm of far-infrared luminosity. Column (5): Logarithm of hard X-ray to far-infrared luminosity ratio. Column (6): Observed q -value. For radio-loud AGNs with extended radio emission, we have adopted the core radio flux. Column (7): Logarithm of infrared luminosity. Column (8): Logarithm of hard X-ray to infrared luminosity ratio. Column (9): Observed q' -value. For radio-loud AGNs with extended radio emission, we have adopted the core radio flux. Column (10): IRAS 25 μm to 60 μm flux ratio. Column (11): Classification. B = broad optical line AGN; N = narrow optical line AGN; U = ultraluminous infrared galaxy, $L_{\text{IR}} > 10^{12} L_{\odot}$ (Sanders & Mirabel 1996).

¹: 1.5 GHz radio flux was estimated from 4.8 GHz radio flux by assuming a radio spectrum of ν^{-1} .

²: 1.5 GHz radio flux was estimated from 2.3 GHz radio flux by assuming a radio spectrum of ν^{-1} .

³: 1.5 GHz radio flux was estimated from 1.4 GHz radio flux by assuming a radio spectrum of ν^{-1} .

⁴: 1.5 GHz radio flux was estimated from 2.3 GHz radio flux by assuming a radio spectrum of ν^0 , since this object shows a flat radio spectrum between 0.8 GHz and 5 GHz (Bransford et al. 1998; Harnett 1987).

⁵: *ASCA* data indicate that the detected hard X-ray emission is a scattered component (Netzer et al. 1998), but Griffiths et al. (1998) estimated the hard X-ray luminosities for both the *Ginga* and *ASCA* data by analyzing the combined *ASCA*, *Ginga*, and *ROSAT* data.

⁶: Netzer et al. (1998) considered the detected hard X-ray spectrum is a scattered component based on its spectral shape. However, the equivalent width of the iron $K\alpha$ emission line is small (~ 100 eV), so we regard this source as the one whose direct hard X-ray emission is detected. The L_X based on *ASCA* data is not available, so we adopted *Ginga* data.

References. — ^a Turner et al. 1997; ^b Nandra & Pounds 1994; ^c Nandra et al. 1997; ^d Elvis et al. 1994; ^e Griffiths et al. 1998; ^f Alonso-Herrero, Ward, & Kotilainen 1997; ^g Iwasawa 1999; ^h Ogasaka et al. 1997; ⁱ Brandt et al. 1997; ^j Rush, Malkan, & Edelson 1996; ^k Bica et al. 1995; ^l Nagar et al. 1999; ^m Dahari & De Robertis 1988; ⁿ Bransford et al. 1998; ^o Wall & Peacock 1985; ^p Condon et al. 1990; ^q Condon 1987; ^r Heisler et al. 1998; ^s Roy et al. 1994; ^t Ulvestad & Wilson 1984; ^u Barvainis, Lonsdale, & Antonucci 1996; ^v Condon et al. 1991b.

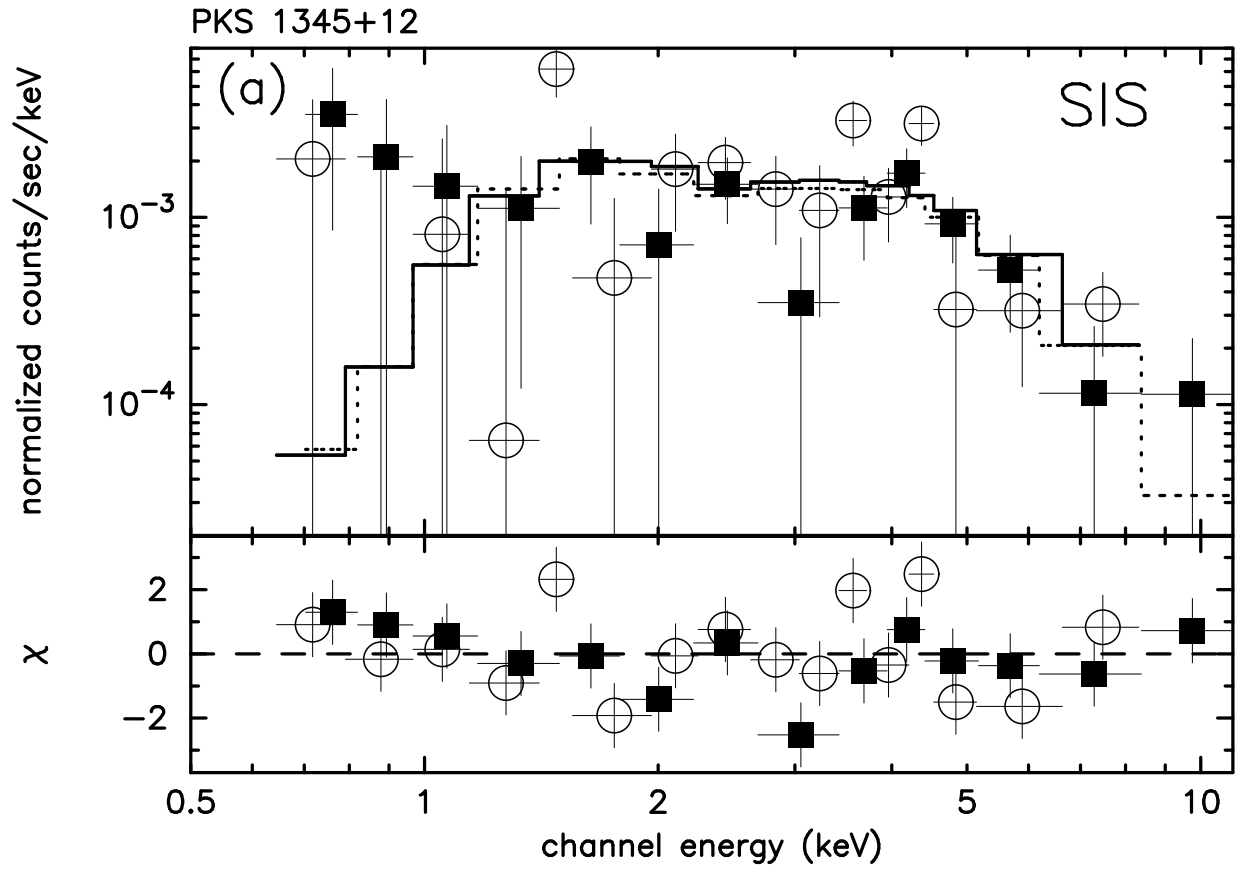


Figure 1a

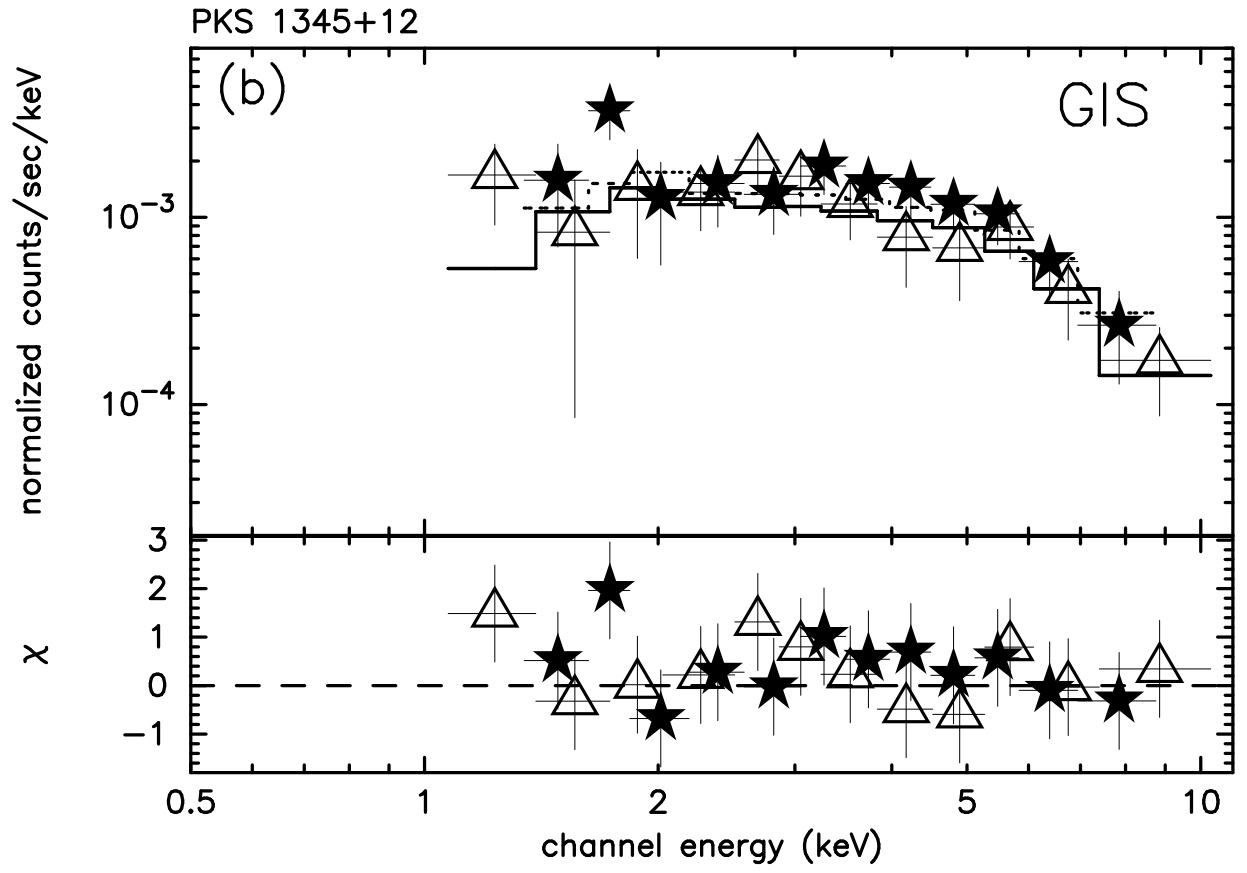


Figure 1b

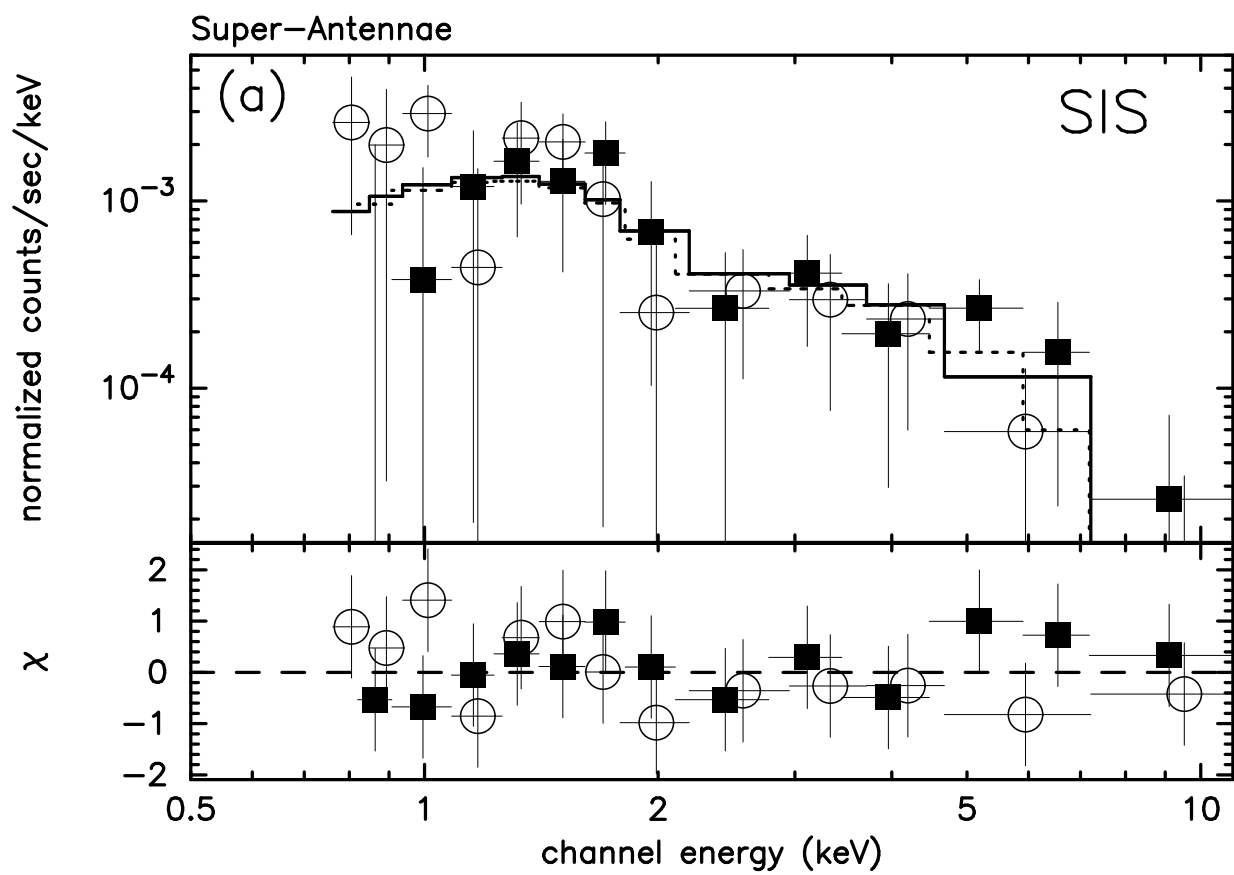


Figure 2a

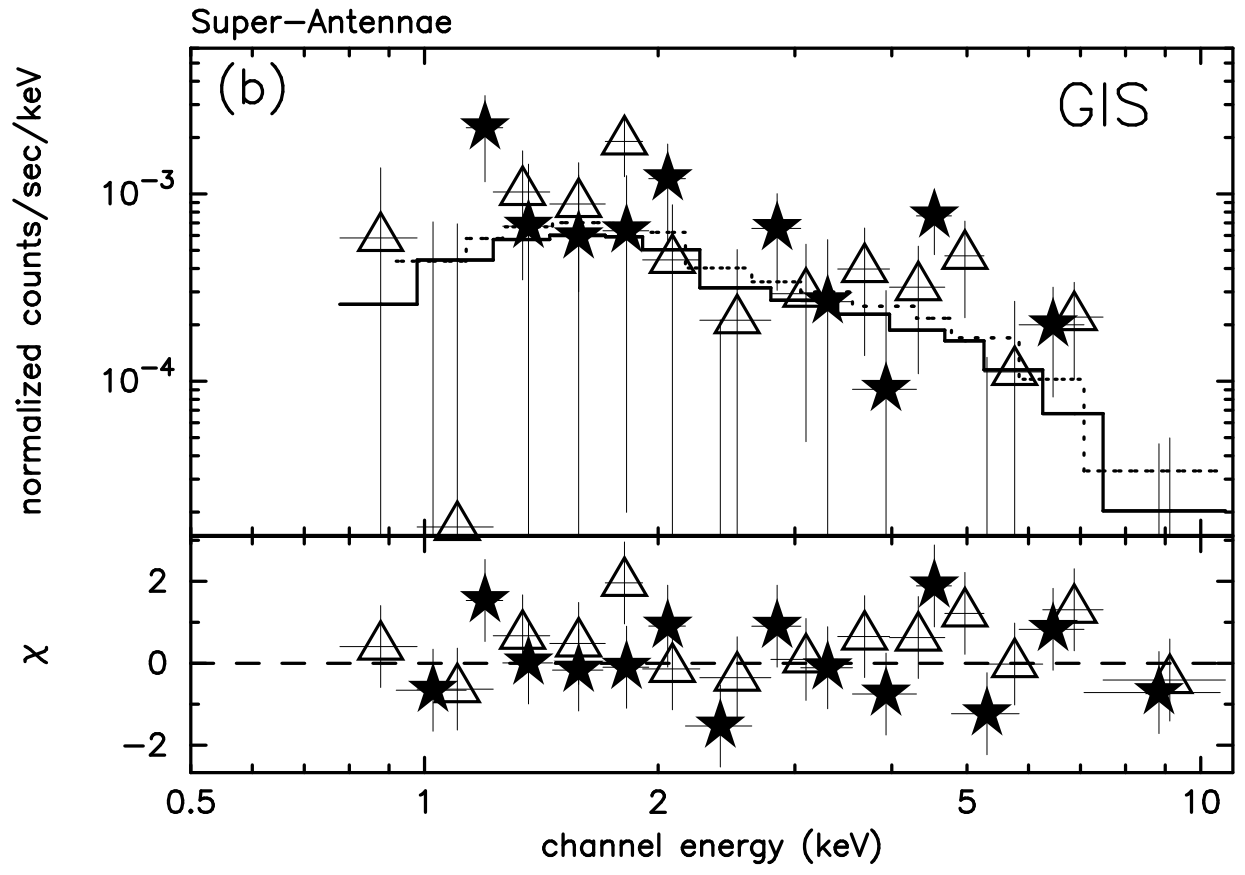


Figure 2b

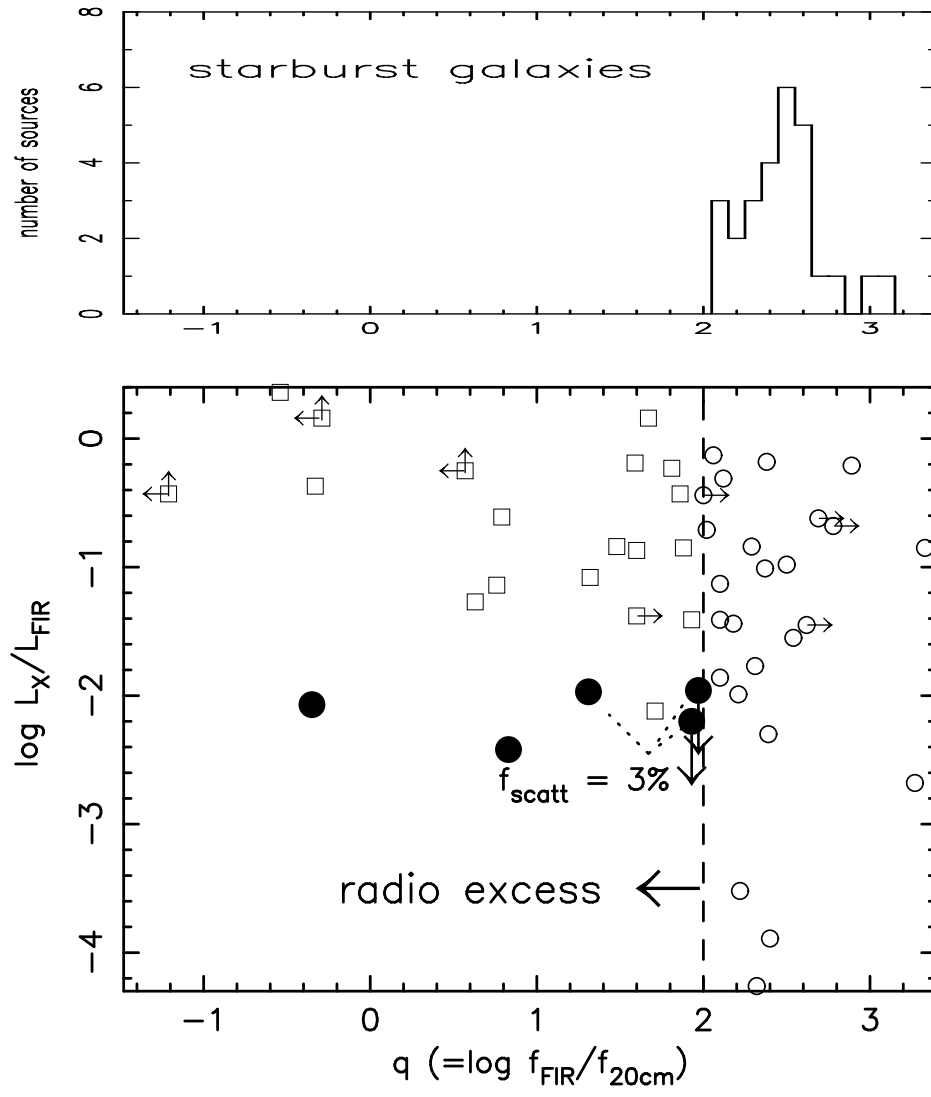


Figure 3

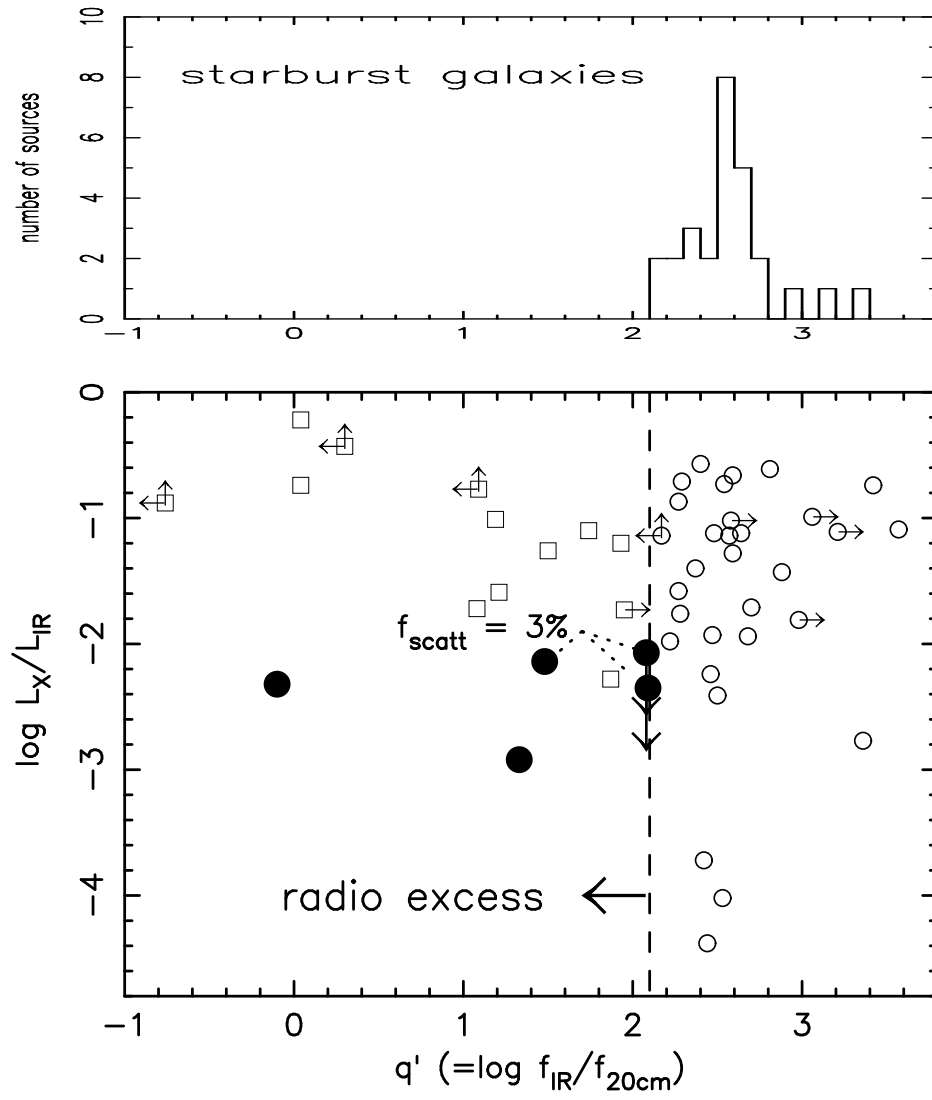


Figure 4